IEEE Access
Multidisciplinary | Rapid Review | Open Access Journal

Received February 11, 2020, accepted March 2, 2020, date of publication March 6, 2020, date of current version March 17, 2020.

Digital Object Identifier 10.1109/ACCESS.2020.2979021

Methodology for High Purity Broadband Near-Unity THz Linear Polarization Converter and Its Switching Characteristics

JIANGUO ZHANG[1], JINPING TIAN[2,3,4], SHUYUAN XIAO[5,6], AND LU LI[1]

[1]Institute of Theoretical Physics, State Key Laboratory of Quantum Optics and Quantum Optics Devices, Shanxi University, Taiyuan 030006, China
[2]College of Physics and Electronics Engineering, Shanxi University, Taiyuan 030006, China
[3]Computer Center, School of Modern Educational Technology, Shanxi University, Taiyuan 030006, China
[4]State Key Laboratory of Integrated Optoelectronics, Institute of Semiconductors, CAS, Beijing 100083, China
[5]Institute for Advanced Study, Nanchang University, Nanchang 330031, China
[6]Jiangxi Key Laboratory for Microscale Interdisciplinary Study, Nanchang University, Nanchang 330031, China

Corresponding authors: Jinping Tian (tianjp@sxu.edu.cn) and Lu Li (llz@sxu.edu.cn)

This work was supported in part by the National Natural Science Foundation of China (NSFC) under Grant 61475198, Grant 61505101, Grant 61775064, Grant 11705108, Grant 11847132, and Grant 11947065, in part by the Natural Science Foundation of Shanxi Province under Grant 201801D121119, in part by the Opened Fund of the State Key Laboratory of Integrated Optoelectronics under Grant IOSKL2019KF16, in part by the Interdisciplinary Innovation Fund of Nanchang University under Grant 2019-9166-27060003, and in part by the Shanxi "1331 Project" Key Subjects Construction (1331KSC).

ABSTRACT Terahertz (THz) polarization converter with high purity of linear polarization conversion, broader conversion band and near-unity conversion efficiency is one of the main research interests in the photonic field. Based on a tri-layer structure of Au, parylene-C and Au, a high purity broadband near-unity THz converter is successfully achieved, and the relative bandwidth (RBW) with polarization conversion ratio (PCR) greater than 98% (90%) can reach about 64.782% (73.094%). The ellipticity is close to zero and the polarization azimuth angle is almost equal to $\pm 90^\circ$ within the frequency range of 1.818$\sim$2.631 THz. These performances originate mainly from the hybridization of the electric excitations and strong coupling effect among the three resonant modes. Besides, the dependencies of conversion performances on the material's electromagnetic parameters and structural parameters are discussed in detail. By selecting metal material with high conductivity and dielectric material with small real and imaginary permittivities, the conversion performances of the proposed converter can be well improved. Meanwhile, the conversion performances are highly robust when the structural parameters change slightly near the optimized value. Finally, the influences of the incident angle and the polarization angle on the conversion performances are also investigated, and the results show that the proposed converter has the characteristics of wide incident angle and polarization angle dependent switching performance. The simple geometry and the better performances make the proposed linear polarization converter a potential candidate in the area of sub-wavelength scale polarization converters, filters, sensors, switches, and so on.

INDEX TERMS High purity, broadband, polarization converter, switching characteristics.

I. INTRODUCTION

Over the past decade, terahertz (THz) radiation has attracted considerable attention in areas of industrial, security, and biomedical applications [1]–[3]. One of the reasons is that it can easily penetrate into objects while posing little destructive risk. However, the development of THz technology is lagging far behind the microwave and optical technologies. In THz science and technology, due to the lack of suitable natural materials, devices based on metamaterials (MMs) are particularly attractive. Naturally, MMs are composed of a layer of metasurface (MS), a layer of dielectric spacer, and a layer of metal substrate. The MS layer is often considered as a two dimensional structure formed by a periodically arranged metal pattern array with sub-wavelength scale, which has also drawn intense interest owing to the highly controllable

The associate editor coordinating the review of this manuscript and approving it for publication was Luyu Zhao.

electromagnetic (EM) response and the excellent performances. Until now, the different types of MSs have been studied extensively in the photonic field. Although numerous THz devices are available, the devices with good performances and low costs, such as absorbers, modulators, optical imaging devices, sensors, polarization converters, photodetectors and thermal emitters, are still worth studying. Specially, THz polarization converters with superior performance are highly expected in advanced sensors, polarization reconfigurable antennas, high sensitive detection, high resolution imaging, liquid crystal display, and many other optical devices.

Using the chirality and anisotropy of MSs, some THz polarization converters operating in reflection (MMs with metal substrate) or transmission (MMs without metal substrate) mode are proposed [4]–[13]. They have the advantage of miniaturization comparing with the conventional polarization converters, such as lenses [14], axicons [15], optical gratings [16], Michelson interferometer [17], photoelastic modulators [18], biasing four-contact photoconductive antenna [19], dichroic crystals [20], and birefringent or anisotropic media [21], [22], etc. However, using MMs to develop converters with broad band and near-unity polarization conversion ratio (PCR) remains a challenging task. In general, the near-unity PCR can be obtained by manipulating simultaneously the effective permittivity and permeability of the MMs [23]–[25], and researchers have been working hard to develop new design strategies or methods to broaden the conversion band [26]–[33]. Among these investigations, the researchers designed different structures and demonstrated different conversion performances by using various methods, for examples, superimposing super-unit cells [26], [27], introducing asymmetric resonances [28], using plasmon hybridization effects [29]–[31], replacing metal resonators with dielectric counterparts [32], and managing phase compensations and dispersion conjugation compensations [33]. However, because these designs are limited by complicated resonator structures, high-cost manufacturing process, bulkier configurations, especially the choice of materials, it is difficult to maintain a high PCR together with a high linear polarization purity within a wide frequency band.

In this paper, we will design a linear polarization converter operating in reflection mode and investigate its conversion performances based on a tri-layer structure composed of patterned Au MS, parylene-C spacer and Au substrate. The parylene-C is a widely used polymer with excellent flexibility and great chemical and biological stability, and its thickness can be precisely controlled by using the chemical vapor deposition (CVD). Moreover, the parylene-C has many specific dielectric properties such as high dielectric strength, low dielectric constant, and low loss. The results show that the converter can not only realize simultaneously the performances of higher linear polarization conversion purity, broadband and near-unity PCR, but also possesses the switching characteristics.

II. STRUCTURE DESIGN, THEORY, AND METHODS

Fig. 1(a) schematically shows the 3D structure diagram of the proposed polarization converter. The top MS layer is an array of L- and C-shaped resonators made of Au with thickness T_1, the dielectric spacer is a thin parylene-C with thickness T_2, and the bottom layer is an Au substrate with thickness T_3. The incident wave and the selected coordinate are also marked in Fig. 1(a). Fig. 1(b) is the top view of a unit cell with its geometric parameters. The C-shaped resonator is a circular arc with center angle of ϕ, radius of r, and its wire width is w_1. The L-shaped resonator has the same arm length l and its wire width is w_2. The array period of the unit cells is denoted as Λ, and s is the distance between the L-shaped resonator and the edge of the unit cell. In this paper, the conductivity of Au is $\sigma_{\mathrm{Au}} = 4.09 \times 10^7$ S/m [34]–[36], and the complex relative permittivity of the parylene-C spacer is $\varepsilon = \varepsilon_{\mathrm{R}} + i\varepsilon_{\mathrm{I}} = 2.42 + i0.0968$ [36] within the operating frequency band. It is worth noting that the electromagnetic parameters of materials are constant unless stated otherwise.

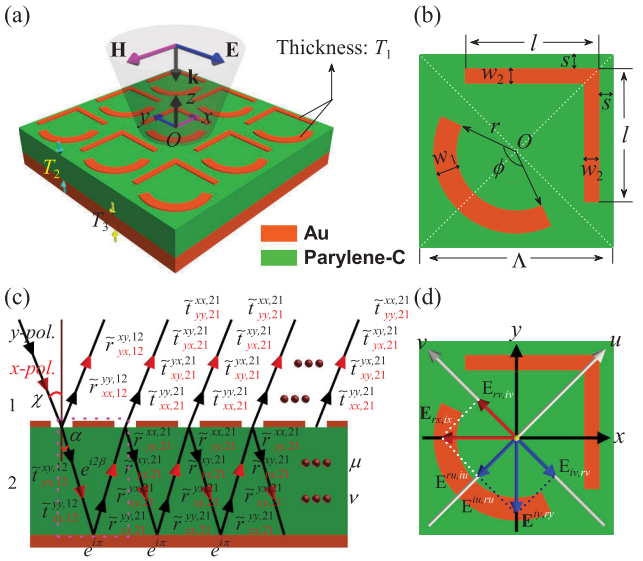

FIGURE 1. (a) Schematic diagram of the proposed polarization converter. A THz plane wave normally illuminates to the top surface of the structure. (b) Top view of a unit cell with all the geometric parameters. (c) Multiple reflection and transmission processes in a Fabry-Pérot-like resonance cavity, where $\tilde{r}$ and $\tilde{t}$ are respectively the reflection and transmission coefficients at different interfaces, and the superscripts and subscripts correspond to the cases of y- and x-polarized waves. (d) Decomposition of linearly polarized incident electric field along x- and y-axes into two orthogonal components along u- and v-axes.

As shown in Fig. 1(a), the bottom metal layer and the top metal pattern form a Fabry-Pérot-like resonance cavity, where the co-polarized or cross-polarized component in the overall reflection field will be enhanced or weakened by the destructive or constructive interferences in the process of multiple reflection and transmission. Hence, we can quantitatively analyze the polarization conversion properties of the proposed structure by the multiple interference theory [37]. As shown in Fig. 1(c), $y(x)$-polarized ($pol.$) waves impinging on the top surface of the converter will be partially reflected

back to air (marked as 1) and partially transmitted into the parylene-C spacer layer (marked as 2). Because of the anisotropy of the proposed MS structure, the reflected waves can be divided into $y(x)$-to-$x(y)$ and $y(x)$-to-$y(x)$ components, where the cross- and co-polarized reflection coefficients can be expressed as $\widetilde{r}^{xy,12}_{yx,12}$ and $\widetilde{r}^{yy,12}_{xx,12}$, respectively. Similarly, the transmitted waves also have $x(y)$- and $y(x)$-polarized components, and the corresponding transmission coefficients can be expressed as $\widetilde{t}^{xy,12}_{yx,12}$ and $\widetilde{t}^{yy,12}_{xx,12}$, respectively. The transmitted waves will continue to propagate in the parylene-C spacer, and will be totally reflected at the bottom metal substrate, then arrive at the top air-converter interface. During the processes, complex phase factors $\exp(i2\beta)$ and $\exp(i\pi)$ will be added due to the existence of the parylene-C spacer and the bottom metal substrate, where $\beta = \sqrt{\varepsilon}k_0T_2/\cos\alpha$, and k_0 is the wavenumber in free space, α is the refraction angle. At the top interface, the y- and x-polarized waves are partially transmitted into air with transmission coefficients $\widetilde{t}^{xy,21}_{yx,21}$, $\widetilde{t}^{yy,21}_{xx,21}$, $\widetilde{t}^{yx,21}_{xy,21}$ and $\widetilde{t}^{xx,21}_{yy,21}$, and partially reflected back again into the parylene-C spacer with reflection coefficients $\widetilde{r}^{xy,21}_{yx,21}$, $\widetilde{r}^{yy,21}_{xx,21}$, $\widetilde{r}^{yx,21}_{xy,21}$ and $\widetilde{r}^{xx,21}_{yy,21}$, and the above process will be repeated. Thus, the electromagnetic waves will shuttle between the top metal pattern and the bottom metal substrate, forming multiple reflection roundtrips, where a roundtrip is marked with a rectangular pink dashed line in Fig. 1(c). The overall reflections for the $y(x)$-to-$x(y)$ and $y(x)$-to-$y(x)$ polarizations can be calculated by the superposition of all reflection roundtrips. For each roundtrip, the corresponding cross-polarized reflection coefficients can be in turn written as:

$$
\begin{aligned}
\widetilde{r}^{xy,0}_{yx,0} &= \widetilde{r}^{xy,12}_{yx,12},\\
\widetilde{r}^{xy,1}_{yx,1} &= \left(\widetilde{t}^{yy,12}_{xx,12}\cdot\widetilde{t}^{xy,21}_{yx,21} + \widetilde{t}^{xy,12}_{yx,12}\cdot\widetilde{t}^{xx,21}_{yy,21}\right)\cdot(-e^{i2\beta}),\\
\widetilde{r}^{xy,2}_{yx,2} &= \left(\widetilde{t}^{yy,12}_{xx,12}\cdot\widetilde{r}^{xy,21}_{yx,21}\cdot\widetilde{t}^{xx,21}_{yy,21} + \widetilde{t}^{yy,12}_{xx,12}\cdot\widetilde{r}^{yy,21}_{xx,21}\cdot\widetilde{t}^{xy,21}_{yx,21}\right.\\
&\quad\left. + \widetilde{t}^{xy,12}_{yx,12}\cdot\widetilde{r}^{xx,21}_{yy,21}\cdot\widetilde{t}^{xx,21}_{yy,21} + \widetilde{t}^{xy,12}_{yx,12}\cdot\widetilde{r}^{yx,21}_{xy,21}\cdot\widetilde{t}^{xy,21}_{yx,21}\right)\\
&\quad\cdot(-e^{i2\beta})^2,\\
\widetilde{r}^{xy,3}_{yx,3} &= \left(\widetilde{t}^{yy,12}_{xx,12}\cdot\widetilde{r}^{xy,21}_{yx,21}\cdot\widetilde{r}^{xx,21}_{yy,21}\cdot\widetilde{t}^{xx,21}_{yy,21}\right.\\
&\quad + \widetilde{t}^{yy,12}_{xx,12}\cdot\widetilde{r}^{xy,21}_{yx,21}\cdot\widetilde{r}^{yx,21}_{xy,21}\cdot\widetilde{t}^{xy,21}_{yx,21}\\
&\quad + \widetilde{t}^{yy,12}_{xx,12}\cdot\widetilde{r}^{yy,21}_{xx,21}\cdot\widetilde{r}^{yx,21}_{xy,21}\cdot\widetilde{t}^{xx,21}_{yy,21}\\
&\quad + \widetilde{t}^{yy,12}_{xx,12}\cdot\widetilde{r}^{yy,21}_{xx,21}\cdot\widetilde{r}^{yy,21}_{xx,21}\cdot\widetilde{t}^{xy,21}_{yx,21}\\
&\quad + \widetilde{t}^{xy,12}_{yx,12}\cdot\widetilde{r}^{xx,21}_{yy,21}\cdot\widetilde{r}^{xx,21}_{yy,21}\cdot\widetilde{t}^{xx,21}_{yy,21}\\
&\quad + \widetilde{t}^{xy,12}_{yx,12}\cdot\widetilde{r}^{xx,21}_{yy,21}\cdot\widetilde{r}^{yx,21}_{xy,21}\cdot\widetilde{t}^{xy,21}_{yx,21}\\
&\quad + \widetilde{t}^{xy,12}_{yx,12}\cdot\widetilde{r}^{yx,21}_{xy,21}\cdot\widetilde{r}^{yx,21}_{yx,21}\cdot\widetilde{t}^{xx,21}_{yy,21}\\
&\quad\left. + \widetilde{t}^{xy,12}_{yx,12}\cdot\widetilde{r}^{yx,21}_{xy,21}\cdot\widetilde{r}^{yy,21}_{xx,21}\cdot\widetilde{t}^{yx,21}_{yx,21}\right)\cdot(-e^{i2\beta})^3,\cdots\cdots.
\end{aligned}
$$

Thus, the overall cross-polarized reflection coefficients can be expressed as:

$$\widetilde{r}^{xy}_{yx} = \sum_{\mu=0}^{\infty}\widetilde{r}^{xy,\mu}_{yx,\mu} \quad (\mu = 0, 1, 2, 3, \ldots\ldots). \tag{1}$$

Similarly, the corresponding co-polarized reflection coefficients for the different roundtrips are:

$$
\begin{aligned}
\widetilde{r}^{yy,0}_{xx,0} &= \widetilde{r}^{yy,12}_{xx,12},\\
\widetilde{r}^{yy,1}_{xx,1} &= \left(\widetilde{t}^{yy,12}_{xx,12}\cdot\widetilde{t}^{yy,21}_{xx,21} + \widetilde{t}^{xy,12}_{yx,12}\cdot\widetilde{t}^{yx,21}_{xy,21}\right)\cdot(-e^{i2\beta}),\\
\widetilde{r}^{yy,2}_{xx,2} &= \left(\widetilde{t}^{yy,12}_{xx,12}\cdot\widetilde{r}^{xy,21}_{yx,21}\cdot\widetilde{t}^{yx,21}_{xy,21} + \widetilde{t}^{yy,12}_{xx,12}\cdot\widetilde{r}^{yy,21}_{xx,21}\cdot\widetilde{t}^{yy,21}_{xx,21}\right.\\
&\quad\left. + \widetilde{t}^{xy,12}_{yx,12}\cdot\widetilde{r}^{xx,21}_{yy,21}\cdot\widetilde{t}^{yx,21}_{xy,21} + \widetilde{t}^{xy,12}_{yx,12}\cdot\widetilde{r}^{yx,21}_{xy,21}\cdot\widetilde{t}^{yy,21}_{xx,21}\right)\\
&\quad\cdot(-e^{i2\beta})^2,\\
\widetilde{r}^{yy,3}_{xx,3} &= \left(\widetilde{t}^{yy,12}_{xx,12}\cdot\widetilde{r}^{xy,21}_{yx,21}\cdot\widetilde{r}^{xx,21}_{yy,21}\cdot\widetilde{t}^{yx,21}_{xy,21}\right.\\
&\quad + \widetilde{t}^{yy,12}_{xx,12}\cdot\widetilde{r}^{xy,21}_{yx,21}\cdot\widetilde{r}^{yx,21}_{xy,21}\cdot\widetilde{t}^{yy,21}_{xx,21}\\
&\quad + \widetilde{t}^{yy,12}_{xx,12}\cdot\widetilde{r}^{yy,21}_{xx,21}\cdot\widetilde{r}^{yx,21}_{xy,21}\cdot\widetilde{t}^{yx,21}_{xy,21}\\
&\quad + \widetilde{t}^{yy,12}_{xx,12}\cdot\widetilde{r}^{yy,21}_{xx,21}\cdot\widetilde{r}^{yy,21}_{xx,21}\cdot\widetilde{t}^{yy,21}_{xx,21}\\
&\quad + \widetilde{t}^{xy,12}_{yx,12}\cdot\widetilde{r}^{xx,21}_{yy,21}\cdot\widetilde{r}^{xx,21}_{yy,21}\cdot\widetilde{t}^{yx,21}_{xy,21}\\
&\quad + \widetilde{t}^{xy,12}_{yx,12}\cdot\widetilde{r}^{xx,21}_{yy,21}\cdot\widetilde{r}^{yx,21}_{xy,21}\cdot\widetilde{t}^{yy,21}_{xx,21}\\
&\quad + \widetilde{t}^{xy,12}_{yx,12}\cdot\widetilde{r}^{yx,21}_{xy,21}\cdot\widetilde{r}^{yx,21}_{yx,21}\cdot\widetilde{t}^{xy,21}_{xy,21}\\
&\quad\left. + \widetilde{t}^{xy,12}_{yx,12}\cdot\widetilde{r}^{yx,21}_{xy,21}\cdot\widetilde{r}^{yy,21}_{xx,21}\cdot\widetilde{t}^{yy,21}_{xx,21}\right)\cdot(-e^{i2\beta})^3,\cdots\cdots,
\end{aligned}
$$

and the overall co-polarized reflection coefficient can be written as:

$$\widetilde{r}^{yy}_{xx} = \sum_{\nu=0}^{\infty}\widetilde{r}^{yy,\nu}_{xx,\nu} \quad (\nu = 0, 1, 2, 3, \ldots\ldots). \tag{2}$$

When the destructive interference occurs between the direct reflection term $[\widetilde{r}^{yy,0}_{xx,0}]$ and other co-polarized reflection terms $[\widetilde{r}^{yy,\nu}_{xx,\nu}\ (\nu = 1, 2, 3, \cdots\cdots)]$, the overall co-polarized reflection amplitude $|\widetilde{r}^{yy}_{xx}|$ may be very small or even disappear. In this case, the cross-polarized reflection amplitude $|\widetilde{r}^{xy}_{yx}|$ will get close to 1, thus the near-unity polarization conversion can be achieved. Note that in Eqs. (1) and (2) there are twenty-four scattering parameters, each of which contains phase and amplitude. These parameters can be obtained through solving the decoupled system (the proposed structure without metal substrate). Thus, the cross-polarized reflection amplitude $|\widetilde{r}^{xy}_{yx}|$ and co-polarized reflection amplitude $|\widetilde{r}^{yy}_{xx}|$ can be theoretically calculated by using Eqs. (1) and (2).

On the other hand, we can directly calculate the cross- and co-polarized reflection amplitudes of the proposed structure by numerical simulations. The numerical simulations are performed in the frequency domain using the EM software CST 2017 based on the standard finite integration technology (FIT). In the simulations, the unit cell boundary condition is used in x- and y-directions and the open (add space) boundary condition is in z-direction.

After obtaining the cross- and co-polarized reflection amplitudes of the proposed structure, the PCR can be calculated by the following formula [38]:

$$\mathrm{PCR}^{y}_{x} = \frac{P_i\left(|\widetilde{r}^{xy}_{yx}|^2\right)}{P_i\left(|\widetilde{r}^{xy}_{yx}|^2 + |\widetilde{r}^{yy}_{xx}|^2\right)} = \frac{|\widetilde{r}^{xy}_{yx}|^2}{|\widetilde{r}^{xy}_{yx}|^2 + |\widetilde{r}^{yy}_{xx}|^2}, \tag{3}$$

where P_i is the power of the incident EM wave. Also, in order to describe the polarization direction of the reflected wave

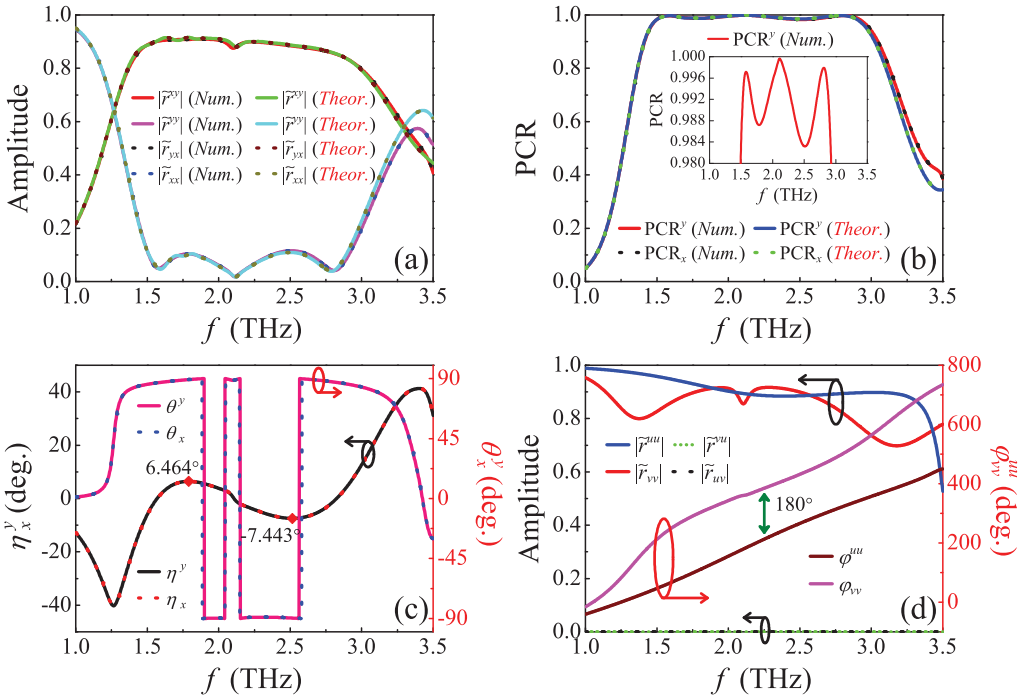

FIGURE 2. (a) Numerically simulated and theoretically calculated cross- and co-polarized reflection amplitudes and (b) PCR for *y*- and *x*-polarized normal incident waves, where the inset is the partially enlarged view of the PCR of *y*-polarized normal incident wave. (c) Polarization azimuth angles θ_x^y and ellipticity η_x^y for the normal incident wave polarized along *y*- or *x*-axis. (d) Simulated reflection amplitudes and phases for *u*- or *v*-polarized normal incident wave.

and the purity of the linear polarization of the proposed converter, we introduce the polarization azimuth angle θ_x^y and ellipticity η_x^y as follows [5], [39]–[42]:

$$\theta_x^y = \frac{1}{2}\tan^{-1}\left[\frac{2|\tau_x^y|\cos(\Delta\varphi_x^y)}{1-|\tau_x^y|^2}\right] = \frac{1}{2}\tan^{-1}\left[\frac{2\,\mathrm{Re}(\tau_x^y)}{1-|\tau_x^y|^2}\right], \tag{4}$$

$$\eta_x^y = \frac{1}{2}\sin^{-1}\left[\frac{2|\tau_x^y|\sin(-\Delta\varphi_x^y)}{1+|\tau_x^y|^2}\right] = \frac{1}{2}\sin^{-1}\left[\frac{2\,\mathrm{Im}(\tau_x^{y*})}{1+|\tau_x^y|^2}\right], \tag{5}$$

where $\tau_x^y = \widetilde{r}_{yx}^{xy}/\widetilde{r}_{xx}^{yy}$, and $\Delta\varphi_x^y = \arg(\widetilde{r}_{yx}^{xy}) - \arg(\widetilde{r}_{xx}^{yy})$ is the phase difference between the $y(x)$ and $x(y)$ components of the reflected wave. Note that θ_x^y and η_x^y are the functions of the frequency. Thus, for a given frequency, if θ_x^y can reach 90° or −90°, then the polarization conversion between the incident and the reflected wave is nearly perfect. As for η_x^y, in general, when $|\eta_x^y| < 10°$, the reflected wave can be considered as a linearly polarized wave [40]–[42], and the smaller $|\eta_x^y|$ is, the higher the linear polarization purity of the reflected wave is. The high degree of linear polarization conversion purity can be used to modify the polarization state in high demanding nonreciprocal response, EM wave isolation and measurement, biomolecular manipulation, polarization selectivity and compatibility, liquid crystal display, and coherent laser beam.

In practice, the L- and C-shaped resonators can be patterned using standard photolithography, metal evaporation and metal lift off. The parylene-C spacer can be fabricated by CVD. The continuous gold substrate can be deposited by electron-beam evaporation. Thus, the whole structure of the proposed converter can be conveniently fabricated with the surface micromachining processes.

III. RESULTS AND DISCUSSIONS

A. POLARIZATION CONVERSION PERFORMANCE UNDER NORMAL INCIDENCE

Firstly, the conversion performances of the proposed converter at normal incidence (i.e., $\chi = 0°$) are investigated. Here, the optimized structural parameters are taken as $\Lambda = 58\ \mu$m, $r = 22.4\ \mu$m, $w_1 = 2.3\ \mu$m, $\phi = 140°$, $s = 4.3\ \mu$m, $w_2 = 2.1\ \mu$m, $l = 29\ \mu$m, $T_1 = 0.5\ \mu$m, $T_2 = 21\ \mu$m, and $T_3 = 0.4\ \mu$m, respectively.

The numerical (*Num.*) simulation and theoretical (*Theor.*) calculation results under normal incidence are presented in Figs. 2(a) and 2(b). One can find that the simulation result is in good agreement with the theoretical prediction. Moreover, it can be clearly seen that $|\widetilde{r}^{xy}|$ is equal to $|\widetilde{r}_{yx}|$, $|\widetilde{r}^{yy}|$ is equal to $|\widetilde{r}_{xx}|$, and PCR^y is equal to PCR_x, which means that the results for the *y*- and *x*-polarized waves are the same. So we only choose the *y*-polarized incident wave in the following discussion. From Fig. 2(a), it can be found that the cross-polarized reflection amplitude $|\widetilde{r}^{xy}|$ is more than 82.613% in a broad frequency region from 1.495 THz to 2.928 THz, and the co-polarized reflection

amplitude $|\widetilde{r}^{yy}|$ is below 12.296%. It is worth noting that the curves of reflection amplitudes have three distinct resonant peaks located at 1.578 THz (mode f_1), 2.151 THz (mode f_2), and 2.810 THz (mode f_3), respectively, which predicts the presence of resonant modes. Particularly, the co-polarized reflectances $|\widetilde{r}^{yy}|^2$ are respectively 0.244%, 0.033%, and 0.170% at the three resonant modes. This means that there is only x-polarized component in the whole reflected waves. In other words, within the frequency band considered, most energy of the y-polarized incident wave is converted to the cross-polarization wave, and the rest is dissipated by the dielectric and metal losses. Fig. 2(b) illustrates the PCR of the incident wave. One can see that, in the frequency range of 1.495 $\sim$ 2.928 THz, the PCR is higher than 98% and even reaches nearly 100% at the three resonant modes. This indicates that the proposed converter can operate at a high conversion efficiency with a wide frequency band. Simultaneously, the relative bandwidth (RBW) [43] of the PCR greater than 98% (90%) can reach about 64.782% (73.094%). Thus the proposed converter exhibits the characteristic of broadband near-unity cross-polarization conversion with high purity. To the best of our knowledge, this result is optimal in the THz frequency band [5], [44]–[47], [50].

The polarization azimuth angle θ_x^y and ellipticity η_x^y given by Eqs. (4) and (5) are shown in Fig. 2(c). One can find that in the frequency range of 1.818 $\sim$ 2.631 THz the ellipticity η_x^y is less than 6.464° and greater than −7.443°. Comparing with the results in the literatures [5], [48]–[50], the range of η_x^y is reduced by more than two times, and the linear polarization purity is obviously improved. Especially, the reflected wave is a pure linearly polarized wave ($\eta_x^y \approx 0$) at 1.578 THz, 2.151 THz, and 2.810 THz. Moreover, the polarization azimuth angle θ_x^y is near −90° in the frequency ranges of 1.893 $\sim$ 2.044 THz and 2.150 $\sim$ 2.571 THz, and is close to 90° around the frequency ranges of 1.495 $\sim$ 1.893 THz, 2.044 $\sim$ 2.150 THz, and 2.571 $\sim$ 2.928 THz. Thus, in the frequency range of 1.495 $\sim$ 2.928 THz, the cross-polarization conversion is always near perfect and is superior to that reported in [5], [10], [12], [48]–[50]. And the comparisons are shown in Table 1. Consequently, the proposed converter can convert the linearly $y(x)$-polarized incident wave to the linearly $x(y)$-polarized reflected wave in a broadband range with high degree of purity.

In order to better understand the linear polarization conversion mechanism, we decompose the incident electric field and the corresponding reflected field into two orthogonal components along 45° directions off y-axis, i.e., u and v axes shown Fig. 1(d). In this way, the $y(x)$-polarized incident field can be decomposed as:

$$\begin{aligned}\mathbf{E}_i &= \mathrm{E}_{ix}^{iy} e^{i(-k_0 z-\omega t)}\widehat{\mathbf{e}}_x^y \\ &= \frac{\sqrt{2}}{2}\mathrm{E}_{ix}^{iy} e^{i(-k_0 z-\omega t)}(\widehat{\mathbf{e}}^u \pm \widehat{\mathbf{e}}_v). \end{aligned} \tag{6}$$

Similarly, the reflected field can be written as:

$$\mathbf{E}_r = \mathrm{E}^{ru} e^{i(k_0 z-\omega t)}\widehat{\mathbf{e}}^u \pm \mathrm{E}_{rv} e^{i(k_0 z-\omega t)}\widehat{\mathbf{e}}_v$$

TABLE 1. Performance comparisons of the proposed polarization converter with previous works.

References	PCR η_x^y	Ranges of η_x^y	Can θ_x^y stay more closer to $\pm 90°$?
[5]	> 90%	$-20.3° \le \eta_x^y \le 23.6°$	Yes
[10]	> 90%	No discussion	No
[12]	> 80%	No discussion	No
[44]	> 80%	No discussion	No discussion
[45]	> 90%	No discussion	No discussion
[46]	> 80%	No discussion	No discussion
[47]	> 80%	No discussion	No discussion
[48]	> 85%	$-22.5° \le \eta_x^y \le 29.8°$	Yes
[49]	> 88%	$-29.9° \le \eta_x^y \le 15.1°$	Yes
[50]	> 85%	$-20.1° \le \eta_x^y \le 20.2°$	Yes
This work	always maintained at above 98% with RBW of 64.782%	$-7.443° \le \eta_x^y \le 6.464°$	Yes

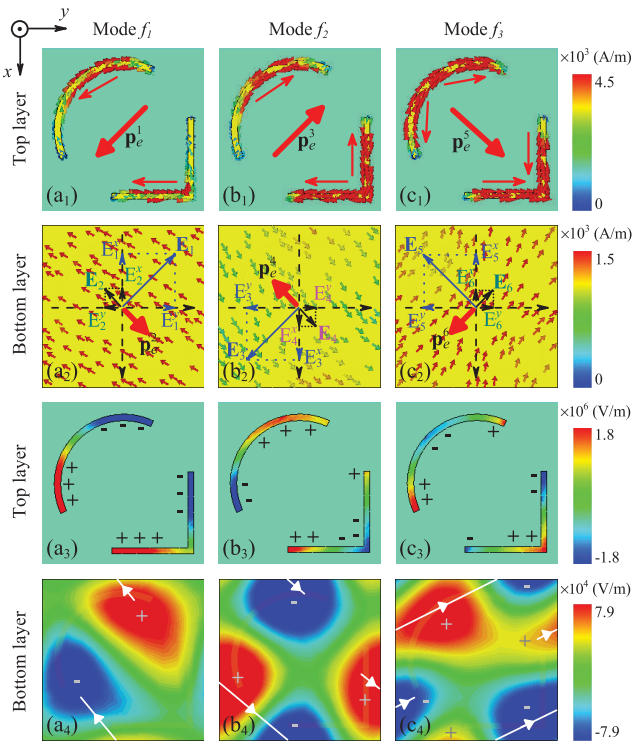

FIGURE 3. Distributions of the induced surface current and the electric field E_z along the top and bottom metal layers at (a) the mode f_1, (b) the mode f_2, and (c) the mode f_3 for the y-polarized normal incident wave, where $\mathbf{p_e}$ is the equivalent electric dipole moment, E is the induced electric field, the signs '+' and '−' indicate the positive and negative charges, and the arrows in (a_4), (b_4) and (c_4) denote the current direction on the bottom layer. Here, the parameters are the same as in Fig. 2.

$$\begin{aligned}&= [|\widetilde{r}^{vu}|\mathrm{E}^{iu} e^{i(k_0 z-\omega t+\varphi^{vu})}\widehat{\mathbf{e}}_v + |\widetilde{r}^{uu}|\mathrm{E}^{iu} e^{i(k_0 z-\omega t+\varphi^{uu})}\widehat{\mathbf{e}}^u] \\ &\quad \pm [|\widetilde{r}_{uv}|\mathrm{E}_{iv} e^{i(k_0 z-\omega t+\varphi_{uv})}\widehat{\mathbf{e}}^u + |\widetilde{r}_{vv}|\mathrm{E}_{iv} e^{i(k_0 z-\omega t+\varphi_{vv})}\widehat{\mathbf{e}}_v] \\ &= |\widetilde{r}^{uu}|\mathrm{E}^{iu} e^{i(k_0 z-\omega t+\varphi^{uu})}\widehat{\mathbf{e}}^u \pm |\widetilde{r}_{vv}|\mathrm{E}_{iv} e^{i(k_0 z-\omega t+\varphi_{vv})}\widehat{\mathbf{e}}_v \\ &= \frac{\sqrt{2}}{2}\mathrm{E}_{ix}^{iy} e^{i(k_0 z-\omega t)}(|\widetilde{r}^{uu}| e^{i\varphi^{uu}}\widehat{\mathbf{e}}^u \pm |\widetilde{r}_{vv}| e^{i\varphi_{vv}}\widehat{\mathbf{e}}_v). \end{aligned} \tag{7}$$

Here, $\widehat{\mathbf{e}}^u$, $\widehat{\mathbf{e}}_v$ and $\widehat{\mathbf{e}}_x^y$ denote the unit vectors in u-axis, v-axis, y-axis, and x-axis. '+' and '−' correspond to the cases of y polarization and x polarization, separately. $\omega = 2\pi f$ is the angular frequency of the incident wave. $\widetilde{r}^{vu}$, $\widetilde{r}^{uu}$, $\widetilde{r}_{uv}$, and $\widetilde{r}_{vv}$ are the cross- and co-polarized reflection coefficients

for u- and v-polarized incidences, respectively. Note that in Eq. (7), $|\widetilde{r}^{vu}| = 0$ and $|\widetilde{r}_{uv}| = 0$ are satisfied, as can be seen from Fig. 2(d). By defining the phase difference between u polarization and v polarization as:

$$\Delta\Phi = \varphi_{vv} - \varphi^{uu}. \tag{8}$$

Eq. (7) can be rewritten as:

$$\mathbf{E}_r = \frac{\sqrt{2}}{2}\mathrm{E}_{ix}^{iy} e^{i(k_0 z - \omega t + \varphi^{uu})}(|\widetilde{r}^{uu}|\widehat{\mathbf{e}}^u \pm |\widetilde{r}_{vv}|e^{i\Delta\Phi}\widehat{\mathbf{e}}_v). \tag{9}$$

From Fig. 2(d), it can be seen that, in the frequency range of 1.495 $\sim$ 2.928 THz, the values of $|\widetilde{r}^{uu}|$ and $|\widetilde{r}_{vv}|$ are very close to each other ($|\widetilde{r}^{uu}| \approx |\widetilde{r}_{vv}|$), and $\Delta\Phi$ is nearly $\pm 180°$. Thus, Eq. (9) can be approximately written as:

$$\begin{aligned}\mathbf{E}_r &\approx \frac{\sqrt{2}}{2}|\widetilde{r}^{uu}|\mathrm{E}_{ix}^{iy} e^{i(k_0 z - \omega t + \varphi^{uu})}(\widehat{\mathbf{e}}^u \mp \widehat{\mathbf{e}}_v) \\ &= |\widetilde{r}^{uu}|\mathrm{E}_{ix}^{iy} e^{i(k_0 z - \omega t + \varphi^{uu})}\widehat{\mathbf{e}}_y^x.\end{aligned} \tag{10}$$

This is consistent with the results of θ_x^y shown in Fig. 2(c). Based on the above derivation processes, we can get three sufficient conditions for converting the $y(x)$-polarized incident wave into the cross-polarized $x(y)$-polarized reflection wave: $|\widetilde{r}^{vu}| \approx |\widetilde{r}_{uv}| \approx 0$, $|\widetilde{r}^{uu}| \approx |\widetilde{r}_{vv}| > 0$, and $\Delta\Phi = (2n+1)\pi$, $(n = 0, \pm 1, \pm 2, \cdots\cdots)$.

The underlying physical mechanism of the polarization conversion can be qualitatively elaborated by the distributions of the induced surface current and the electric field along the top and bottom metal layers at the three resonant modes, as shown in Fig. 3. Figs. 3(a_1) and 3(a_3) show the distribution of the instantaneous induced surface current and the electric field on the top layer at mode f_1. One can see that the positive and negative charges are mainly distributed at both ends of the L- and C-shaped resonators, thus forming two electric dipoles and the equivalent electric dipole moment can be denoted as $\mathbf{p}_e^1$. At the same time, as shown in Figs. 3(a_2) and 3(a_4), the induced surface current on the bottom layer will cause another equivalent electric dipole moment $\mathbf{p}_e^2$. Then the two equivalent electric dipole moments $\mathbf{p}_e^1$ and $\mathbf{p}_e^2$ will lead to two induced electric fields $\mathbf{E}_1$ and $\mathbf{E}_2$, and as shown in Fig. 3(a_2), the combination of these two induced electric field can be written as:

$$\mathbf{E}^1 = \left(\mathrm{E}^{x1}, \mathrm{E}^{y1}\right) = \mathbf{E}_1 + \mathbf{E}_2 = \left(-\mathrm{E}_1^x - \mathrm{E}_2^x, \mathrm{E}_1^y - \mathrm{E}_2^y\right),$$

Obviously, one can see that the magnitude of E^{x1} is much larger than that of E^{y1}. Thus, for the y-polarized incident wave, the reflected wave at mode f_1 is mainly along $-x$-axis, and at this time, one will have $\theta^y(f_1) \approx 90°$, as shown in Fig. 2(c).

Similarly, at modes f_2 and f_3, the surface currents on the top layer and on the bottom layer can cause equivalent electric dipole moments $\mathbf{p}_e^3$, $\mathbf{p}_e^4$, $\mathbf{p}_e^5$ and $\mathbf{p}_e^6$. Their combinations will respectively lead to the induced electric fields $\mathbf{E}^3$ and $\mathbf{E}^4$ at mode f_2, $\mathbf{E}^5$ and $\mathbf{E}^6$ at mode f_3, as shown in Figs. 3(b) and 3(c). But, the location and way of the accumulation of the positive and negative charges in the L- and C-shaped resonators are very different from those at mode f_1, as can be seen in Figs. 3(b_3) and 3(c_3). So the directions of the currents and the equivalent electric dipole moments are different, as shown in Figs. 3(b_1), 3(c_1), 3(b_2) and 3(c_2). In the cases, the combined induced electric fields at modes f_2 and f_3 can be respectively expressed as:

$$\begin{aligned}\mathbf{E}^2 &= \left(\mathrm{E}^{x2}, \mathrm{E}^{y2}\right) = \mathbf{E}_3 + \mathbf{E}_4 = \left(\mathrm{E}_3^x + \mathrm{E}_4^x, \mathrm{E}_4^y - \mathrm{E}_3^y\right), \\ \mathbf{E}^3 &= \left(\mathrm{E}^{x3}, \mathrm{E}^{y3}\right) = \mathbf{E}_5 + \mathbf{E}_6 = \left(-\mathrm{E}_5^x - \mathrm{E}_6^x, \mathrm{E}_6^y - \mathrm{E}_5^y\right).\end{aligned}$$

It is clear that the magnitude of E^{x2} (E^{x3}) is much larger than that of E^{y2} (E^{y3}). So the cross-polarization conversions are dominant at modes f_2 and f_3, and the corresponding reflected waves are mainly along x- and $-x$-axes, respectively. Therefore, at these two modes, $\theta^y(f_2) \approx -90°$ and $\theta^y(f_3) \approx 90°$, as shown in Fig. 2(c).

Note that Fig. 3 discussed only the conversion mechanism at the three resonant modes. In fact, our results showed that the higher PCR can be kept in a broad frequency range, as shown in Fig. 2(c), which means that there exists strong coupling effects among the resonant modes. In addition, it should be pointed out that the reason why the theoretically calculated results are almost identical to the numerically simulated results is that the polarization conversion in the proposed converter results mainly from the electric excitations (i.e., there is no magnetic excitation in the structure).

B. VARIATIONS OF CONVERSION PERFORMANCE AGAINST MATERIAL'S ELECTROMAGNETIC PARAMETERS

In this subsection, we discuss the effect of electromagnetic parameters of materials on the polarization conversion of the proposed converter. Figs. 4 and 5 depict the numerically simulated and theoretically calculated cross- and co-polarized reflection amplitudes ($|\widetilde{r}^{xy}|$ and $|\widetilde{r}^{yy}|$) and PCR^y as well as the ellipticity η^y and polarization azimuth angle θ^y of the y-polarized normal incident wave for various metals and different real and imaginary parts of the permittivity of the dielectric spacer layer. It is clear that the theoretically calculated results ($|\widetilde{r}^{xy}|$, $|\widetilde{r}^{yy}|$, and PCR^y) are in well agreement with the numerically simulated ones.

Figs. 4(a) and 5(a) are the results for various metallic materials taken as Cr, Al-Si-Mg alloy, Pb, Au and Ag with conductivities 2.2×10^5 S/m, 4.09×10^5 S/m, 5.0×10^6 S/m, 4.09×10^7 S/m and 6.06×10^7 S/m [34]–[36], [51]–[53]. It can be seen from Figs. 4(a_1) and 4(a_3) that, with the increasing of conductivity, the cross-polarization reflection amplitude $|\widetilde{r}^{xy}|$ will increase in different degree accompanied by the broadening of the conversion bandwidth and the increasing of PCR^y. As for η^y and θ^y, with the increase of conductivity, the frequency band with $|\eta^y| < 10°$ and $\theta^y \approx \pm 90°$ are increased, which means that higher purity of linear polarization conversion appeared in a wider frequency band, as shown in Figs. 5(a_1) and 5(a_2-a_6). As a result, the metallic materials with higher conductivities will have better broadband conversion characteristics than those with lower conductivities,

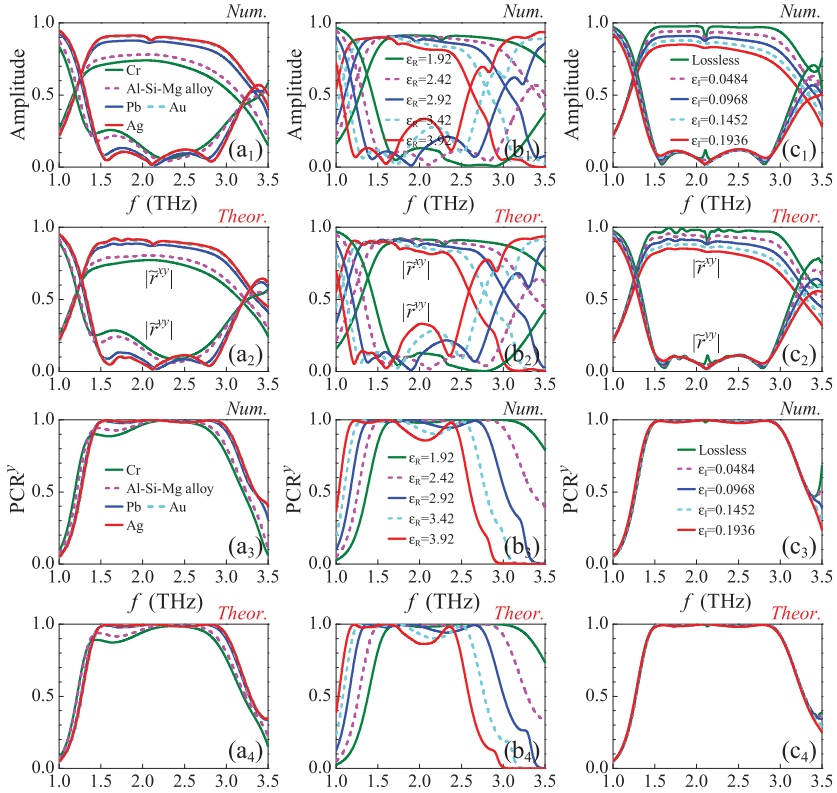

FIGURE 4. Cross- and co-polarized reflection amplitudes and PCR^y of the *y*-polarized normal incident wave for (a) various metals, (b) different real parts and (c) different imaginary parts of the permittivity of the dielectric spacer, where the subscripts 1 and 3 are the numerically simulated results, 2 and 4 are the theoretically calculated results. Here, the other parameters are the same as in Fig. 2.

and this is helpful for selecting proper metallic material in the design of linear polarization converters with higher purity and higher efficiency.

Figs. 4(b) and 5(b) display the results for different real part ε_R of the permittivity of the spacer layer. One can find that, with the increase of ε_R, all the curves are red-shifted. Meanwhile, the conversion bandwidth with higher efficiency and higher purity of linear polarization is narrower. The results showed that, the smaller the value of ε_R, the better the broadband conversion efficiency and the higher the linear polarization conversion purity.

Figs. 4(c) and 5(c) show the results for different imaginary part ε_I of the permittivity of the spacer layer. With the increase of ε_I, $|\widetilde{r}^{xy}|$ decreases obviously, but $|\widetilde{r}^{yy}|$ increases slightly, as shown in Figs. 4(c_1) and 4(c_2). Meanwhile, the values of PCR^y remains almost unchanged in a wide frequency band, as shown in Figs. 4(c_3) and 4(c_4). Also, the change of ε_I has little influence on the ellipticity $|\eta^y|$, see Fig. 5(c_1), but has obvious influence on the polarization azimuth angle θ^y. As shown in Figs. 5(c_2-c_6), the smaller the value of ε_I, the broader the bandwidth with $\theta^y \approx \pm 90°$. Thus, high-efficiency broadband conversion and higher purity of linear polarization conversion can be achieved by reducing the dielectric loss.

In brief, based on the above optimized design of the higher efficiency and higher purity of broadband linear polarization converter from the perspective of electromagnetic properties of materials, we selected Au as the metal layers and parylene-C as the dielectric spacer in our design.

C. EFFECTS OF THE STRUCTURAL PARAMETERS ON THE POLARIZATION CONVERSION

It is well known that MMs are structure-dependent EM materials. Therefore, it is essential to analyze the robustness of the structural parameters' influence on the conversion performances of the proposed converter. In this subsection, as examples, we will study the influences of four structural parameters (w_1, w_2, ϕ, l) on the cross- and co-polarized reflection amplitudes and PCR^y for *y*-polarized normal incident wave, and the results are summarized in Fig. 6. The first column of Fig. 6 shows in turn the simulated cross- and co-polarized reflection amplitudes for different w_1, w_2, ϕ, and l. The right two columns are respectively the numerically simulated and the theoretically calculated PCR^y. It is obvious that, with the increase of these parameters, the resonant mode f_1 or f_3 will have different degrees of red-shift or blue-shift. For examples, the resonant mode f_1 is red-shifted

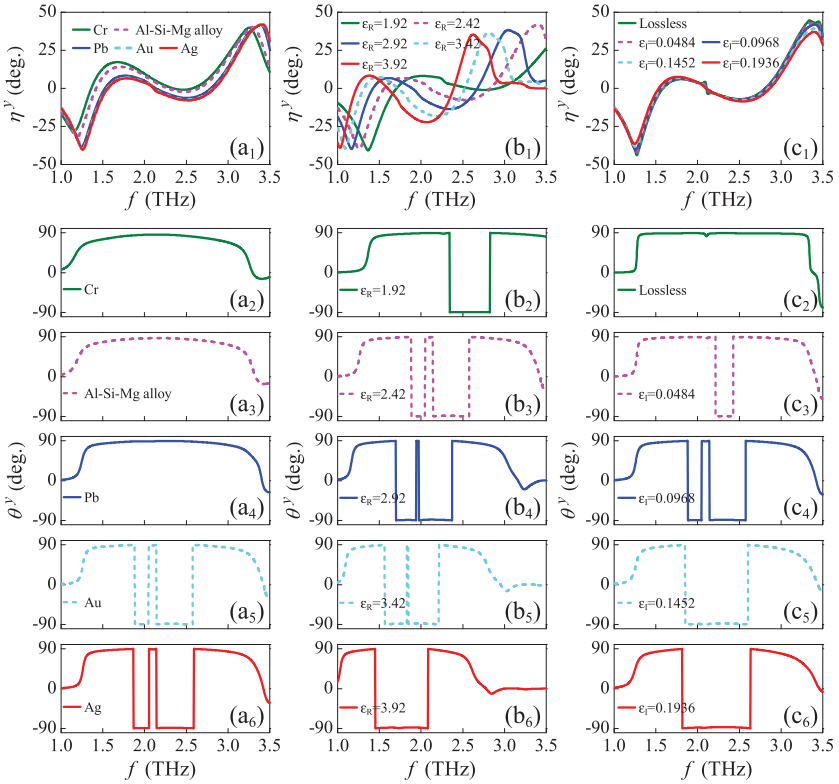

FIGURE 5. Ellipticity η^y and polarization azimuth angle θ^y of the y-polarized normal incident wave for (a) various metals, (b) different real parts and (c) different imaginary parts of the permittivity of the dielectric spacer, where the subscript 1 is for η^y, and the subscripts 2-6 are for θ^y. Here, the other parameters are the same as in Fig. 2.

in Figs. 6(a_1), 6(c_1) and 6(d_1) and the resonant mode f_3 is blue-shifted in Figs. 6(a_1) and 6(b_1). The result will lead to the broadening of the conversion band. At the same time, high PCR^y can be maintained in the broadband, as shown in the second column in Fig. 6. Furthermore, one can find that, if the optimized structural parameters are used, i.e., $w_1 = 2.3\ \mu$m, $w_2 = 2.1\ \mu$m, $\phi = 140°$, and $l = 29\ \mu$m, the slight changes with them will not cause significant changes in $|\widetilde{r}^{xy}|$, $|\widetilde{r}^{yy}|$, and PCR^y. This means that the polarization conversion and broadband characteristics of the proposed converter have good tolerance and robustness to small changes in the optimized structural parameters. However, a large deviation from them will have different degrees of influence on the conversion efficiency, such as the cases of $w_1 = 5.3$ and $6.3\ \mu$m in Fig. 6(a), the cases of $w_2 = 3.6$ and $4.1\ \mu$m in Fig. 6(b), the case of $\phi = 150°$ in Fig. 6(c), and the case of $l = 31\ \mu$m in Fig. 6(d). In these cases, although the conversion bands are wider, the conversion efficiencies have different degrees of reduction. Thus the tradeoff between the conversion efficiency and bandwidth is a key issue in the optimization process of the structural parameters. In short, the conversion efficiency and bandwidth of the proposed converter are dependent on the structural parameters, and each parameter of the C- and L-shaped resonators will have a different influence on them. However, the proposed converter is highly robust against the minor changes of the optimized structural parameters.

D. CHARACTERISTICS OF WIDE INCIDENT ANGLE AND POLARIZATION ANGLE DEPENDENT SWITCHING

In the previous subsections, we investigated the polarization conversion performances of the proposed converter for the normal incident y-polarized wave. In this subsection, we will study the influences of incident angle χ and polarization angle ψ on the conversion performance of the optimized converter.

Firstly, we discuss the influences of incident angle χ on the conversion performance as $\psi = 0°$. The numerically simulated and theoretically calculated PCR versus χ are presented in Fig. 7 for both TE and TM incident waves, respectively. It can be seen clearly that the theoretically calculated results are nearly consistent with the numerically simulated ones within the effective conversion frequency bands. Here, TE and TM waves correspond respectively to the cases of the electric field along y-axis and x-axis [54], [55]. For TE wave, as shown in Fig. 7(a), higher PCR can be maintained in a broader conversion band when the incident angle χ varies from 0° to 20°. When χ is larger than 20°, the conversion band will split, and both the conversion efficiency and the bandwidths decrease slightly. As for TM wave, it is more

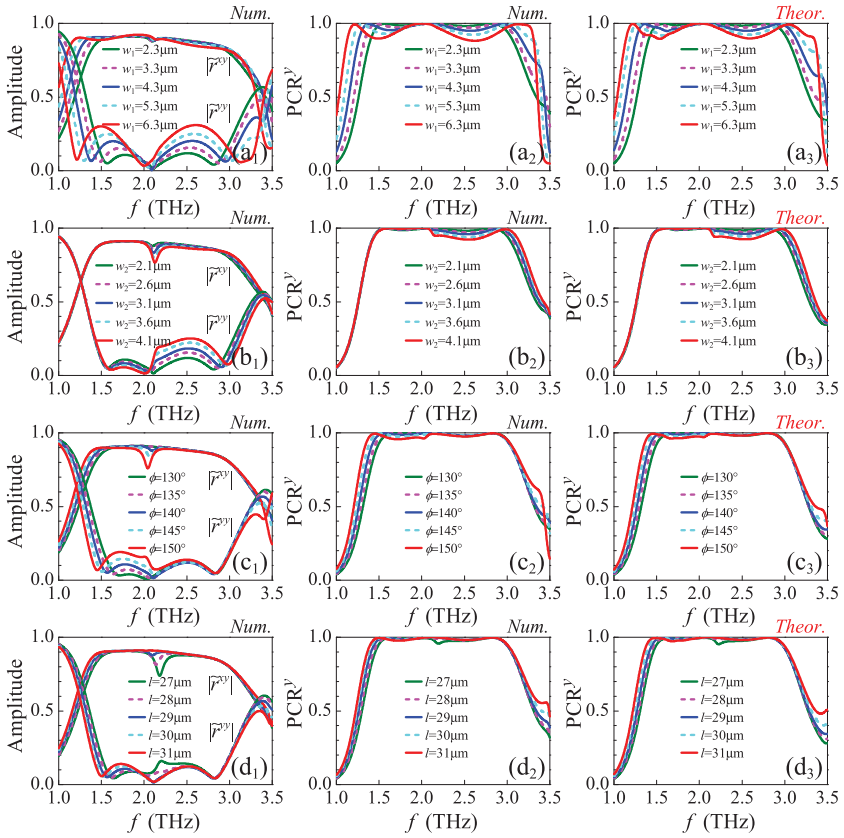

FIGURE 6. Influences of the structural parameters on the cross- and co-polarized reflection amplitudes and PCR^y for the y-polarized normal incident wave. (a) the wire width w_1 of the C-shaped resonator, (b) the wire width w_2 of the L-shaped resonator, (c) the central angle ϕ of the C-shaped resonator, and (d) the lateral arm length l of the L-shaped resonator, and the subscripts 1 and 2 are the numerically simulated results and the subscript 3 is the theoretically calculated result for PCR^y. Here, the other parameters are the same as in Fig. 2.

insensitive to the incident angle than TE wave. The incident angle range of broader band and higher PCR is up to 40°, as shown in Fig. 7(b). When χ is greater than 40°, the conversion band will also split, while the conversion efficiency can be still maintained at a high level.

In order to have an intuitive understanding for the conversion band splitting, let us look back at Fig. 1(c). One can see that, at first, the optical path of an obliquely incident EM wave in the parylene-C spacer is larger than that of a vertically incident wave, and it will increase with the increase of the incident angle, leading to increasing propagating loss. Secondly, the complex propagating phase of a roundtrip in the spacer layer can be expressed as $2\beta = 2\sqrt{\varepsilon}k_0T_2/\cos\alpha$, and the superposed complex propagating phase after multiple reflection will approximately satisfy the destructive interference condition at the top surface of the proposed structure when the incident angle is lager than about 20° for TE incident waves. Thirdly, the propagating phase is also greater than that under normal incidence, which will provide additional propagating phase and create extra resonance between the top and bottom metallic layers, leading to the absorption of incident TE waves. Just because these three points, the band splitting of PCR and conversion efficiency reduction happened at around 2 THz [56], [57]. However, one can also find that these changes are not so obvious for TM incident waves because we have shown that the electric resonance plays major roles in the proposed polarization converter. In brief, this wide incident angle characteristic is beneficial to the practical application, and it should be pointed out that the values of PCR are the same when $\psi = 0°$, 90°, 180°, 270°, and 360°.

In the following, we will demonstrate the polarization angle-dependent switching characteristics under the case of $\chi = 0°$. Fig. 8 presents the conversion properties of the proposed converter with the varying polarization angle ψ. From Fig. 8(a), one can see that the cross-polarized reflection amplitude exhibits a periodic variation behavior with the increase of ψ. Specifically, it decreases gradually from maximum to minimum when ψ changes from 0° to 45°, then increases again to the maximum as ψ continues to increase to 90°. This process will be repeated. However, the periodic variation behavior of the co-polarized reflection amplitude is different from that of the cross-polarized reflection, as observed in Fig. 8(b). Consequently, the change of PCR

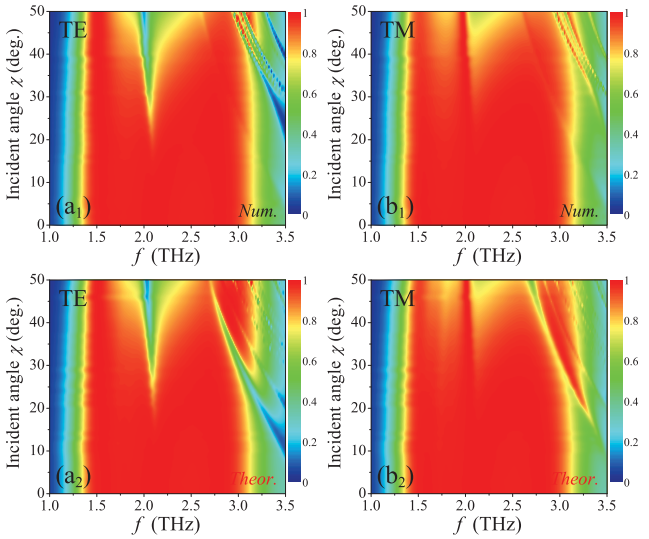

FIGURE 7. Dependence of PCR on the incident angles χ for (a) TE wave and (b) TM wave when the polarization angle is equal to 0°. The subscripts 1 and 2 in figures correspond respectively to the numerically simulated and theoretically calculated results. Here, the other parameters are the same as in Fig. 2.

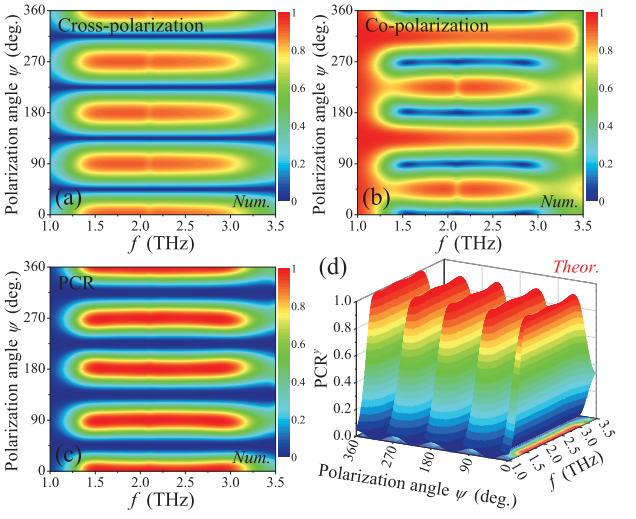

FIGURE 8. Dependence of the numerically simulated cross-polarized reflection amplitudes (a), co-polarized reflection amplitudes (b), PCR (c), and the theoretically calculated PCR (d) on the polarization angles for normal incident wave. Here, the other parameters are the same as in Fig. 2.

with the varying polarization angle is also periodic, as shown in Figs. 8(c) and 8(d).

The periodic variation behavior may be reasonably explained by the instantaneous induced surface current distributions. In fact, as explained in Fig. 3, when $\psi = 0°$, i.e., for y-polarized incident wave, the cross-polarization conversion is dominant, resulting in peak PCR. The result is also valid for the cases of $\psi = 90°$, 180°, and 270°. However, when $\psi = 45°$, 135°, 225°, and 315°, the results will be different. As examples, we present the simulation results for the cases

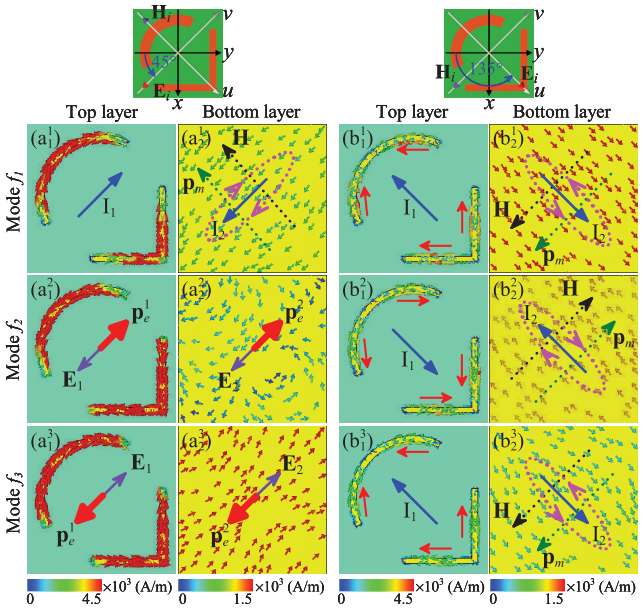

FIGURE 9. Distributions of the induced surface current along the top and bottom metallic layers at the modes f_1, f_2, and f_3 when (a) $\psi = 45°$ and (b) $\psi = 135°$, where $\mathbf{p}_e$, $\mathbf{E}$, $\mathbf{p}_m$ and $\mathbf{H}$ are the electric dipole moment, induced electric field, magnetic moment and induced magnetic field, respectively, and the subscripts 1 and 2 are the cases of the top and bottom layers. Here, the other parameters are the same as in Fig. 2.

of $\psi = 45°$ and 135° in Fig. 9. It can be found from Figs. 9(a_1^1) and 9(a_2^1) that when $\psi = 45°$, the directions of currents I_1 and I_2 on the top and bottom layers are opposite at mode f_1, thus an induced magnetic field $\mathbf{H}$ will be generated due to the formation of a circulating current loop between the top and bottom layers, which is parallel to the incident magnetic field $\mathbf{H}_i$. As for the modes f_2 and f_3, as shown in Figs. 9(a_2^1), 9(a_2^2), 9(a_3^1) and 9(a_3^2), the induced electric fields $\mathbf{E}_1$ and $\mathbf{E}_2$ are parallel to the incident electric field $\mathbf{E}_i$. So there is only co-polarization conversion with PCR= 0 when $\psi = 45°$. When $\psi = 135°$, the physical mechanisms at the three modes are similar to those shown in Figs. 9(a_1^1) and 9(a_2^1), and one can find that the induced magnetic fields are parallel to the incident magnetic field. So there are also no cross-polarization conversions at this time and PCR= 0 is valid. Besides, one can also achieve the same results analytically according to the aforementioned field decomposition theory. However, when the polarization direction deviates from these specific angles, the induced magnetic fields and electric fields will have both contributions to the cross- and co-polarizations. Therefore, with the change of polarization angle, the behavior of PCR will change periodically, as shown in Figs. 8(c) and 8(d).

The periodic variation of PCR indicates that the proposed polarization converter has polarization angle dependent switching characteristics. That is to say, the states with PCR reaching its maximum when the polarization angle of incident electromagnetic wave is equal to 0°, 90°, 180°, 270°, and 360° can be regarded as 'on' states, while the 'off' states correspond to the cases when the polarization angle

is 45°, 135°, 225°, and 315°. Consequently, the switching performance can be achieved in a broader conversion band by adjusting the polarization angle of the incident wave. So the proposed converter is polarization-sensitive, and its switching characteristic may be applied to the field of MMs switching, which expands the application area of the polarization converter and is helpful to the design of sub-wavelength MMs devices.

IV. CONCLUSION

In summary, based on the classical tri-layer MMs structure, a linear polarization converter was proposed. The study results have shown that the relative bandwidth (RBW) with PCR greater than 98% (90%) can reach about 64.782% (73.094%). The ellipticity η_x^y is close to zero and the polarization azimuth angle θ_x^y is very close to $\pm 90°$ within the frequency range $1.818 \sim 2.631$ THz. These results indicated that the proposed converter can realize high efficient conversion from $y(x)$-polarized incident wave to $x(y)$-polarized reflected one with high degree of purity. These performances can be attributed to the hybridization of the electric excitations and strong mutual coupling effect between the adjacent resonant modes. Furthermore, the dependencies of the conversion performances on the material's electromagnetic parameters and the structural parameters have been analyzed in detail. It has been found that the higher the conductivity of the metal materials, or the smaller the real and imaginary parts of the dielectric materials, the higher the purity and the efficiency of the broadband converter. At the same time, one can also find that the conversion performances are highly robust against the small variation of the optimized structural parameters. Finally, the influences of the incident angle and the polarization angle on the conversion performances have also been investigated, and the results indicated that the optimized converter has a good tolerance to the incident angle whether the incident wave is TE or TM polarization when the polarization angle is 0°, 90°, 180°, and 270°. In addition, the proposed converter possesses the polarization angle-dependent switching characteristic. The numerical simulation results are in agreement with the theoretical calculation results based on multiple interference theory. The proposed structure is simple and can be easily fabricated in practical applications, which is helpful to construct other high efficient broadband MMs devices, such as wave plates, optical switches, optical isolators, absorbers, MMs antennas, and so on.

ACKNOWLEDGMENT

The author Jianguo Zhang would like to acknowledge Dr. Menglin L. N. Chen (University of Hong Kong) and Prof. Wei E. I. Sha (Zhejiang University) for the valuable discussions.

REFERENCES

[1] F. M. Al-Douseri, Y. Chen, and X.-C. Zhang, "THz wave sensing for petroleum industrial applications," *Int. J. Infr. Millim. Waves*, vol. 27, no. 4, pp. 481–503, Apr. 2006.

[2] J. F. Federici, B. Schulkin, F. Huang, D. Gary, R. Barat, F. Oliveira, and D. Zimdars, "THz imaging and sensing for security applications–explosives, weapons and drugs," *Semicond. Sci. Technol.*, vol. 20, no. 7, pp. S266–S280, Jun. 2005.

[3] X. Yang, X. Zhao, K. Yang, Y. Liu, Y. Liu, W. Fu, and Y. Luo, "Biomedical applications of terahertz spectroscopy and imaging," *Trends Biotechnol.*, vol. 34, no. 10, pp. 810–824, Oct. 2016.

[4] X. Yu, X. Gao, W. Qiao, L. Wen, and W. Yang, "Broadband tunable polarization converter realized by graphene-based metamaterial," *IEEE Photon. Technol. Lett.*, vol. 28, no. 21, pp. 2399–2402, Nov. 2016.

[5] Z. Xiao, H. Zou, X. Zheng, X. Ling, and L. Wang, "A tunable reflective polarization converter based on hybrid metamaterial," *Opt. Quantum Electron.*, vol. 49, no. 12, p. 401, Nov. 2017.

[6] J. Zhu, S. Li, L. Deng, C. Zhang, Y. Yang, and H. Zhu, "Broadband tunable terahertz polarization converter based on a sinusoidally-slotted graphene metamaterial," *Opt. Mater. Express*, vol. 8, no. 5, p. 1164, Apr. 2018.

[7] L. Peng, X.-F. Li, X. Jiang, and S.-M. Li, "A novel THz half-wave polarization converter for cross-polarization conversions of both linear and circular polarizations and polarization conversion ratio regulating by graphene," *J. Lightw. Technol.*, vol. 36, no. 19, pp. 4250–4258, Oct. 1, 2018.

[8] V. S. Yadav, S. K. Ghosh, S. Bhattacharyya, and S. Das, "Graphene-based metasurface for a tunable broadband terahertz cross-polarization converter over a wide angle of incidence," *Appl. Opt.*, vol. 57, no. 29, pp. 8720–8726, Oct. 2018.

[9] V. S. Yadav, S. K. Ghosh, S. Das, and S. Bhattacharyya, "Wideband tunable mid-infrared cross-polarisation converter using monolayered graphene-based metasurface over a wide angle of incidence," *IET Microw., Antennas Propag.*, vol. 13, no. 1, pp. 82–87, Jan. 2019.

[10] W. Liu, S. Chen, Z. Li, H. Cheng, P. Yu, J. Li, and J. Tian, "Realization of broadband cross-polarization conversion in transmission mode in the terahertz region using a single-layer metasurface," *Opt. Lett.*, vol. 40, no. 13, pp. 3185–3188, Jun. 2015.

[11] X. Zang, S. Liu, Q. Cheng, J. Xie, Y. Zhu, and Y. Wang, "Lower-order-symmetry induced bandwidth-controllable terahertz polarization converter," *J. Opt.*, vol. 19, no. 11, Oct. 2017, Art. no. 115103.

[12] L. Dai, Y. Zhang, H. Zhang, and J. F. O'Hara, "Broadband tunable terahertz cross-polarization converter based on dirac semimetals," *Appl. Phys. Express*, vol. 12, no. 7, Jun. 2019, Art. no. 075003.

[13] Z. Cheng and Y. Cheng, "A multi-functional polarization convertor based on chiral metamaterial for terahertz waves," *Opt. Commun.*, vol. 435, pp. 178–182, Mar. 2019.

[14] B. Scherger, C. Jördens, and M. Koch, "Variable-focus terahertz lens," *Opt. Express*, vol. 19, no. 5, pp. 4528–4535, Feb. 2011.

[15] Z. Wu, X. Wang, W. Sun, S. Feng, P. Han, J. Ye, and Y. Zhang, "Vector characterization of zero-order terahertz bessel beams with linear and circular polarizations," *Sci. Rep.*, vol. 7, no. 1, p. 13929, Oct. 2017.

[16] I. Yamada, K. Takano, M. Hangyo, M. Saito, and W. Watanabe, "Terahertz wire-grid polarizers with micrometer-pitch al gratings," *Opt. Lett.*, vol. 34, no. 3, p. 274, Jan. 2009.

[17] R. Shimano, H. Nishimura, and T. Sato, "Frequency tunable circular polarization control of terahertz radiation," *Jpn. J. Appl. Phys.*, vol. 44, no. 21, pp. L676–L678, May 2005.

[18] J. Badoz, M. Billardon, J. C. Canit, and M. F. Russel, "Sensitive devices to determine the state and degree of polarization of a light beam using a birefringence modulator," *J. Opt.*, vol. 8, no. 6, pp. 373–384, Dec. 1977.

[19] Y. Hirota, R. Hattori, M. Tani, and M. Hangyo, "Polarization modulation of terahertz electromagnetic radiation by four-contact photoconductive antenna," *Opt. Express*, vol. 14, no. 10, p. 4486, May. 2006.

[20] C.-Y. Chen, T.-R. Tsai, C.-L. Pan, and R.-P. Pan, "Room temperature terahertz phase shifter based on magnetically controlled birefringence in liquid crystals," *Appl. Phys. Lett.*, vol. 83, no. 22, pp. 4497–4499, Dec. 2003.

[21] L. Zhang, H. Zhong, C. Deng, C. Zhang, and Y. Zhao, "Characterization of birefringent material using polarization-controlled terahertz spectroscopy," *Opt. Express*, vol. 18, no. 19, p. 20491, Sep. 2010.

[22] T. Meissner and F. J. Wentz, "Polarization rotation and the third Stokes parameter: The effects of spacecraft attitude and Faraday rotation," *IEEE Trans. Geosci. Remote Sens.*, vol. 44, no. 3, pp. 506–515, Mar. 2006.

[23] H. Tao, W. J. Padilla, X. Zhang, and R. D. Averitt, "Recent progress in electromagnetic metamaterial devices for terahertz applications," *IEEE J. Sel. Topics Quantum Electron.*, vol. 17, no. 1, pp. 92–101, Jan. 2011.

[24] Y. Liu and X. Zhang, "Metamaterials: A new frontier of science and technology," *Chem. Soc. Rev.*, vol. 40, no. 5, pp. 2494–2507, Nov. 2011.

[25] C. L. Holloway, E. F. Kuester, J. A. Gordon, J. O'Hara, J. Booth, and D. R. Smith, "An overview of the theory and applications of metasurfaces: The two-dimensional equivalents of metamaterials," *IEEE Antennas Propag. Mag.*, vol. 54, no. 2, pp. 10–35, Apr. 2012.
[26] Y. Cheng, R. Gong, and L. Wu, "Ultra-broadband linear polarization conversion via diode-like asymmetric transmission with composite metamaterial for terahertz waves," *Plasmonics*, vol. 12, no. 4, pp. 1113–1120, Aug. 2017.
[27] X.-F. Zang, S.-J. Liu, H.-H. Gong, Y. Wang, and Y.-M. Zhu, "Dual-band superposition induced broadband terahertz linear-to-circular polarization converter," *J. Opt. Soc. Amer. B, Opt. Phys.*, vol. 35, no. 4, p. 950, Mar. 2018.
[28] Y.-J. Chiang and T.-J. Yen, "A composite-metamaterial-based terahertz-wave polarization rotator with an ultrathin thickness, an excellent conversion ratio, and enhanced transmission," *Appl. Phys. Lett.*, vol. 102, no. 1, Jan. 2013, Art. no. 011129.
[29] X. Wen and J. Zheng, "Broadband THz reflective polarization rotator by multiple plasmon resonances," *Opt. Express*, vol. 22, no. 23, p. 28292, Nov. 2014.
[30] C. Yang, Y. Luo, J. Guo, Y. Pu, D. He, Y. Jiang, J. Xu, and Z. Liu, "Wideband tunable mid-infrared cross polarization converter using rectangle-shape perforated graphene," *Opt. Express*, vol. 24, no. 15, p. 16913, Jul. 2016.
[31] M. Chen, L. Z. Chang, X. Gao, H. Chen, C. Y. Wang, X. F. Xiao, and D. P. Zhao, "Wideband tunable cross polarization converter based on a graphene metasurface with a hollow-carved 'H' array," *IEEE Photon. J.*, vol. 9, no. 5, Oct. 2017, Art. no. 4601011.
[32] Q. Yang, X. Chen, Q. Xu, C. Tian, Y. Xu, L. Cong, X. Zhang, Y. Li, C. Zhang, X. Zhang, J. Han, and W. Zhang, "Broadband terahertz rotator with an all-dielectric metasurface," *Photon. Res.*, vol. 6, no. 11, pp. 1056–1061, Oct. 2018.
[33] X. Gao, W. Yang, W. Cao, M. Chen, Y. Jiang, X. Yu, and H. Li, "Bandwidth broadening of a graphene-based circular polarization converter by phase compensation," *Opt. Express*, vol. 25, no. 20, pp. 23945–23954, Sep. 2017.
[34] B.-X. Wang, G.-Z. Wang, and L.-L. Wang, "Design of a novel dual-band terahertz metamaterial absorber," *Plasmonics*, vol. 11, no. 2, pp. 523–530, Sep. 2016.
[35] J. F. Wu, B. H. Ng, H. D. Liang, M. B. H. Breese, M. H. Hong, S. A. Maier, H. O. Moser, and O. Hess, "Chiral metafoils for terahertz broadband high-contrast flexible circular polarizers," *Phys. Rev. A,* vol. 2, no. 1, Jul. 2014, Art. no. 014005.
[36] Y. Wen, W. Ma, J. Bailey, G. Matmon, X. Yu, and G. Aeppli, "Planar broadband and high absorption metamaterial using single nested resonator at terahertz frequencies," *Opt. Lett.*, vol. 39, no. 6, pp. 1589–1592, Mar. 2014.
[37] N. K. Grady, J. E. Heyes, D. R. Chowdhury, Y. Zeng, M. T. Reiten, A. K. Azad, A. J. Taylor, D. A. R. Dalvit, and H.-T. Chen, "Terahertz metamaterials for linear polarization conversion and anomalous refraction," *Science*, vol. 340, no. 6138, pp. 1304–1307, May 2013.
[38] J. Hao, Y. Yuan, L. Ran, T. Jiang, J. A. Kong, C. T. Chan, and L. Zhou, "Manipulating electromagnetic wave polarizations by anisotropic metamaterials," *Phys. Rev. Lett.*, vol. 99, no. 6, Aug. 2007, Art. no. 063908.
[39] M. Akbari, M. Farahani, A.-R. Sebak, and T. A. Denidni, "Ka-band linear to circular polarization converter based on multilayer slab with broadband performance," *IEEE Access*, vol. 5, pp. 17927–17937, 2017.
[40] J. C. Zhao and Y. Z. Cheng, "Ultra-broadband and high-efficiency reflective linear polarization convertor based on planar anisotropic metamaterial in microwave region," *Optik*, vol. 136, pp. 52–57, May 2017.
[41] J. Chen, H. Yang, G. Zhang, X. Huang, S. Hu, Q. Chen, and H. Lin, "Integrating an ultra-broadband power splitter and a polarization converter using a zigzag metamaterial," *Opt. Mater. Express*, vol. 8, no. 6, p. 1454, May 2018.
[42] X. J. Huang, B. X. Xiao, D. Yang, and H. L. Yang, "Ultra-broadband 90° polarization rotator based on bi-anisotropic metamaterial," *Opt. Commun.*, vol. 338, pp. 416–421, Nov. 2015.
[43] X. Gao, L. Singh, W. Yang, J. Zheng, H. Li, and W. Zhang, "Bandwidth broadening of a linear polarization converter by near-field metasurface coupling," *Sci. Rep.*, vol. 7, no. 1, p. 6817, Jul. 2017.
[44] Y. Z. Cheng, W. Withayachumnankul, A. Upadhyay, D. Headland, Y. Nie, R. Z. Gong, M. Bhaskaran, S. Sriram, and D. Abbott, "Ultrabroadband reflective polarization convertor for terahertz waves," *Appl. Phys. Lett.*, vol. 105, no. 18, Nov. 2014, Art. no. 181111.
[45] F. Luo, F. Lan, Z. Yang, Z. Shi, L. Meng, H. Su, and M. Shi, "Multiband terahertz reflective polarizer based on asymmetric L-shaped split-ring-resonators metasurface," in *Proc. 11th Int. Symp. Antennas, Propag. EM Theory (ISAPE)*, Oct. 2016, pp. 905–907.
[46] J. Zhao, Y. Cheng, and Z. Cheng, "Design of a photo-excited switchable broadband reflective linear polarization conversion metasurface for terahertz waves," *IEEE Photon. J.*, vol. 10, no. 1, Feb. 2018, Art. no. 4600210.
[47] W. Pan, D.-J. Shen, and Y.-J. Yan, "Design of broadband polarization converter for terahertz waves," *Optoelectronics Lett.*, vol. 14, no. 6, pp. 434–437, Dec. 2018.
[48] H. Shi, J. Li, A. Zhang, J. Wang, and Z. Xu, "Broadband cross polarization converter using plasmon hybridizations in a ring/disk cavity," *Opt. Express*, vol. 22, no. 17, pp. 20973–20981, Aug. 2014.
[49] J. C. Zhao and Y. Z. Cheng, "A high-efficiency and broadband reflective 90° linear polarization rotator based on anisotropic metamaterial," *Appl. Phys. B, Lasers Opt.*, vol. 122, no. 10, p. 255, Sep. 2016.
[50] R. Xia, X. Jing, X. Gui, Y. Tian, and Z. Hong, "Broadband terahertz half-wave plate based on anisotropic polarization conversion metamaterials," *Opt. Mater. Express*, vol. 7, no. 3, pp. 977–988, Feb. 2017.
[51] D. Hu, H. Wang, Z. Tang, and X. Zhang, "Investigation of a broadband refractory metal metamaterial absorber at terahertz frequencies," *Appl. Opt.*, vol. 55, no. 19, pp. 5257–5262, Jun. 2016.
[52] B.-X. Wang, L.-L. Wang, G.-Z. Wang, W.-Q. Huang, X.-F. Li, and X. Zhai, "A simple design of a broadband, polarization-insensitive, and low-conductivity alloy metamaterial absorber," *Appl. Phys. Express*, vol. 7, no. 8, Jul. 2014, Art. no. 082601.
[53] T. Meng, D. Hu, H. Wang, X. Zhang, and Z. Tang, "Theoretical investigation of a five-band terahertz absorber based on an asymmetric split-ring resonator," *Appl. Opt.*, vol. 56, no. 34, pp. 9601–9605, Dec. 2017.
[54] J. Zhang, J. Tian, and L. Li, "A dual-band tunable metamaterial near-unity absorber composed of periodic cross and disk graphene arrays," *IEEE Photon. J.*, vol. 10, no. 2, pp. 1–12, Apr. 2018, Art. no. 4800512.
[55] J. Zhang, J. Tian, and L. Li, "Pantoscopic and temperature-controlled dual-band perfect absorber based on strontium titanate material," *Mater. Res. Express*, vol. 5, no. 6, Jun. 2018, Art. no. 065802.
[56] F. Li, L. Zhang, P. Zhou, H. Chen, R. Zhao, Y. Zhou, D. Liang, H. Lu, and L. Deng, "Dual-band reflective polarization converter based on slotted wire resonators," *Appl. Phys. B, Lasers Opt.*, vol. 124, no. 2, p. 28, Jan. 2018.
[57] M. Diem, T. Koschny, and C. M. Soukoulis, "Wide-angle perfect absorber/thermal emitter in the terahertz regime," *Phys. Rev. B, Condens. Matter*, vol. 79, no. 3, Jan. 2009, Art. no. 033101.

JIANGUO ZHANG received the B.S. degree in physics from Jinzhong University, Jinzhong, China, in 2014. He is currently pursuing the Ph.D. degree in theoretical physics with the Institute of Theoretical Physics, Shanxi University, Taiyuan, China. His research interests include metamaterials/metasurfaces, topological photonics, 2D material nanophotonics, and active devices in the terahertz frequency region.

JINPING TIAN was born in Shuozhou, China, in 1975. He received the B.S. degree in electronics and information system and the Ph.D. degree in optics from Shanxi University, Taiyuan, China, in 1997 and 2006, respectively. He is currently a Professor with the College of Physics and Electronics Engineering, Shanxi University. His research interests include theoretical analysis of optical soliton, nanophotonic and plasmonic devices, and metamaterial devices.

SHUYUAN XIAO received the B.S. degree in physics from Central China Normal University, Wuhan, China, in 2012, the M.S. degree in theoretical physics from Southwest University, Chongqing, China, in 2015, and the Ph.D. degree in optical engineering from Wuhan National Laboratory for Optoelectronics, Huazhong University of Science and Technology, Wuhan, in 2018. In 2019, he joined the Institute for Advanced Study, Nanchang University, Nanchang, China, where he is currently a Research Fellow. His research interests include plasmonics, metamaterials, 2D material nanophotonics, and active devices.

LU LI was born in Datong, China, in 1960. He received the Ph.D. degree from Shanxi University. He is currently a Professor with the Institute of Theoretical Physics, Shanxi University. His current research interests include optical soliton, optical communications, and electromagnetic metamaterials.